Chemical Engineering Science 163 (2017) 105–113

Contents lists available at ScienceDirect

Chemical Engineering Science

journal homepage: www.elsevier.com/locate/ces

The lag between micro- and macro-mixing in compressed fluid flows

Daniel Bassing [a,b], Andreas S. Braeuer [a,c,*]

[a] Erlangen Graduate School in Advanced Optical Technologies (SAOT), Friedrich-Alexander-Universität Erlangen-Nürnberg (FAU), Germany
[b] Lehrstuhl für Prozessmaschinen und Anlagentechnik (iPAT), Friedrich-Alexander-Universität Erlangen-Nürnberg (FAU), Germany
[c] Lehrstuhl für Technische Thermodynamik (LTT), Friedrich-Alexander-Universität Erlangen-Nürnberg (FAU), Germany

HIGHLIGHTS

- Simultaneous remote composition analysis on micro- and macro-scale.
- Based on spat. and temp. resolved one-dimensional *in situ* Raman spectroscopy.
- Lag between macro- and micro-mixing quantified spatially resolved.
- Lag between macro- and micro-mixing quantified along a line.

GRAPHICAL ABSTRACT

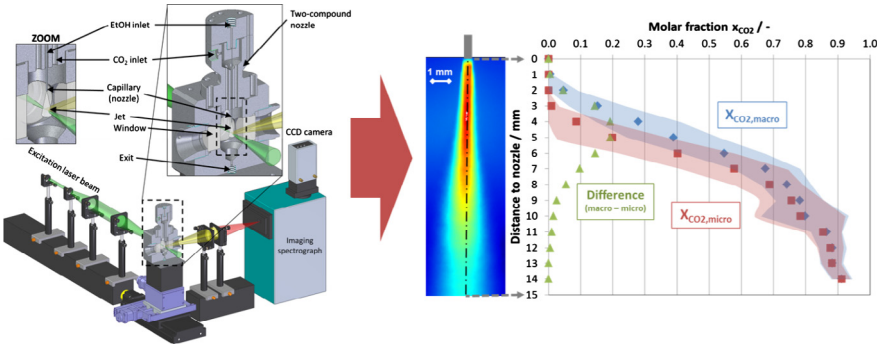

ARTICLE INFO

Article history:
Received 12 September 2016
Received in revised form 22 December 2016
Accepted 15 January 2017
Available online 17 January 2017

Keywords:
Micro-mixing
Macro-mixing
Hydrogen bond
Raman
Compressed fluid
High-pressure
Supercritical fluid

ABSTRACT

We report the application of a novel optical Raman-based measurement technique for the simultaneous determination of the progress of mixing on the micro- and on the macro-scale. The introduced measurement technique is applicable to mixing systems containing one compound, which potentially can form hydrogen bonds, such as water, alcohols or amines, and does not rely on the addition of traces of indicator compounds. Here we demonstrate its applicability by analyzing the lag of micro-mixing behind macro-mixing when liquid ethanol is injected into a supercritical bulk environment mainly composed of carbon dioxide (CO_2). While the degree of mixing on the macro-scale is determined from the ratio of the intensities of characteristic Raman signals of ethanol and CO_2, the degree of mixing on the micro-scale is determined from the shape of the O—H stretching vibration Raman signal of ethanol, which is a function of the development of hydrogen bonds.

1. Introduction

Mixing is a crucial step for many process technologies. Reactions or precipitation mechanisms are governed by interactions between molecules and thus are largely determined by the degree of mixing on a molecular level (micro-scale), which is not easily accessible with conventional measurement techniques. Therefore we here present a Raman-based measurement technique which simultaneously probes the degree of mixing on the micro- as well as on the macro-scale.

In rocket (Mayer et al., 2000; Roy et al., 2013) and internal combustion engines (Falgout et al., 2016; Wensing et al., 2015) as well as in hydrothermal flames (Meier et al., 2016) for spallation drilling (Rothenfluh et al., 2011) or waste water treatment (Wellig et al., 2009; Queiroz et al., 2015), the fuel and the oxidizer have to be

* Corresponding author at: Erlangen Graduate School in Advanced Optical Technologies (SAOT), Friedrich-Alexander-Universität Erlangen-Nürnberg (FAU), Germany.
E-mail address: andreas.braeuer@fau.de (A.S. Braeuer).

http://dx.doi.org/10.1016/j.ces.2017.01.034
0009-2509/

mixed before the onset of the combustion. Different "particles-from-sprays" processes, which also take place at elevated pressure, rely on a fast mixing of either a solution with a blowing agent (Liparoti et al., 2015), a solution with an antisolvent (Braeuer et al., 2011) or an emulsion with an extraction agent (Kluge et al., 2009). For the generation of polyurethane foams the isocyanate and the carbon dioxide (CO_2) containing polyol have to be mixed homogeneously before the initialization of the polymerization and the solidification of the foam (Michaeli and Heinz, 2000). All these processes have in common that they take place at elevated pressure, up to 25 MPa. Considering the critical parameters of example pure compounds, which are for water 647.1 K & 22.1 MPa, for CO_2 304.2 K & 7.4 MPa, for nitrogen 126.2 K & 3.4 MPa and for ethanol 514 K & 6.3 MPa, it becomes obvious that these compounds and mixtures of them are treated at conditions at which they feature a considerable compressibility and thus at elevated pressures can be said to be compressed.

Compressed fluids – here we use the wording "fluid" as we do not want to specify the fluid's state as either gaseous, supercritical or eventually liquid – feature a kinematic viscosity ν which regarding its value exceeds that of the mass diffusivity D. Therefore the dimensionless Schmidt number

$$Sc = \frac{\nu}{D} \tag{1}$$

of compressed fluids is usually between $Sc \approx 1$ for non-compressed gases and $Sc > 100$ for liquids. The Schmidt number of a fluid in the vicinity of its critical point is usually $Sc \approx 10$. Physically, the Schmidt number relates the thickness of the hydrodynamic mixing layer to the thickness of the mass transfer layer. While the thickness of the hydrodynamic mixing layer is proportional to the kinematic viscosity, the thickness of the mass transfer layer is proportional to the diffusivity. The hydrodynamic mixing layer is the layer containing the velocity gradient between two fluids A and B flowing with different velocities. The mass transfer layer is the layer containing the composition gradient between two fluids A and B of different composition. Turbulent hydrodynamic mixing layers break down into eddies, which again break down into smaller and smaller eddies (Richardson, 1922), until a smallest size scale, the so called Kolmogorov scale, is reached at which the eddy's rotational energy is dissipated (Kolmogorov, 1941; Davidson, 2004). As long as eddies rotate, the thickness of the hydrodynamic mixing layers between the eddies and the surrounding fluid is still determined by the viscosity. At the time when the eddies cease to rotate, the velocity gradient between the previous eddy structure and the surrounding fluid becomes zero and thus also the hydrodynamic mixing layer disappears, while the mass transfer layer remains. Assuming the hypothetic case that there is no mass diffusion during the flow-driven macro-mixing, then the smallest eddy structures would still contain solely fluid A and would be surrounded by fluid B. Such a state we refer to as macroscopically mixed, but microscopically not-mixed. Macroscopic mixing is determined by the viscosity and by the flow, while microscopic mixing is solely governed by the mass diffusivity and homogenizes the mixture on a molecular level. Summarizing, for many non-compressed gases, for which $Sc \approx 1$ we therefore can assume that at the time when the fluids A and B are mixed on a macro-scale, they are also mixed on a micro-scale. Such a system would not feature composition heterogeneities on a micro-scale, when it is already homogeneous on a macro-scale. This is different for liquids, where $Sc > 100$ describes that mass diffusion is still ongoing at times when macroscopic mixing is already over. Such a system would feature long-living composition heterogeneities on a micro-scale when it is already homogeneous on the macro-scale. For compressed fluids the situation is in between. The lifetime (time-scale) of the obtained micro-scale heterogeneities can be longer than the reaction time in diesel combustion or the nucleation time in precipitation processes. This implies that reactions or particle nucleation can start in systems which are not yet homogeneously mixed on the micro-scale. Then the prevailing composition heterogeneities on the micro-scale, which spread over the entire mixture, make homogeneous reaction or nucleation conditions impossible, which influences also the reaction products and the generated particles. There will be regions in which fluid A and B are mixed on a molecular level, regions in which they are not yet mixed and regions in which the mixture state is in between. In other words, the micro-scale heterogeneities can in principle be translated into the heterogeneities of the products made with any high pressure process containing compressed fluids, if the product formation starts in a system still heterogeneous on the micro-scale.

Fig. 1 shows the detection section of a typical planar laser diagnostics experiment for the analysis of the mixing processes taking place in a hypothetic jet-mixing experiment. Here a "black" fluid is injected as a jet into a "white" bulk fluid. In the jet mixing zone downstream the nozzle the black and the white fluids mix. The cross section of the jet, which is irradiated by the planar light sheet is imaged via one lens onto a charged coupled device (CCD)-detector. One pixel of the CCD-chip is enlarged as an insert and decorated with a question mark in Fig. 1. The pixel is filled grey which is supposed to indicate that at this location in the illuminated cross section of the jet, one can find 50% of the black fluid and 50% of the white fluid, together resulting in grey.

Unfortunately, due to the limited spatial resolution of measurement techniques, no information can be extracted on the degree of mixing below the spatial resolution limit. The hypothetic mixing states I to VI in Fig. 1 all represent scenarios where one would find equal portions of black and white fluid. But only state I shows a scenario in which the two fluids are really mixed. States II to VI represent scenarios which are macroscopically mixed, but are not yet mixed on a micro-scale. State VI can for example represent a structure of a previous Kolmogorov scale eddy which is still visible just because diffusion is so slow that the relaxed eddy structure still contains only the black fluid.

Therefore the spatial resolution of measurement techniques, which usually is above the scale of the micro heterogeneities, makes a direct investigation into micro-mixing impossible. In fact, techniques which potentially can analyze micro-mixing must rely on probing phenomena taking place beyond their spatial resolution, so on the molecular scale. Thus, known methods rely on the addition of substances acting either as pH-indicator (Koochesfahani and Dimotakis, 1986; Lehwald et al., 2010), as energy transfer indicator (Yip et al., 1994; Braeuer et al., 2011) or as educts for consecutive competing reactions (Baldyga and Bourne, 1989; Kling and Mewes, 2004; Bałdyga and Bourne, 1999). Unfortunately this is not an option for processes operated close to the critical parameters of the fluids treated in them, as these processes are rather sensitive towards minor modifications. The addition of traces of indicator-substances could heavily affect the thermodynamics, the fluid properties and with this mixing and mass transfer.

On this purpose we developed a non-invasive tracer-free and remote measurement technique which *in situ* probes simultaneously the degree of micro- and macro-mixing in an example turbulent jet mixing experiment. The jet mixing configuration is in the style of that of the supercritical antisolvent (SAS) technique for the generation of fine particles from compressed fluid systems (Braeuer et al., 2011); certainly here without the formation of particles, as micro- and macro-mixing is in the focus of this study instead of particle formation. The decisive advantage of the here presented Raman method is that no indicator-substance has to be added to the fluids. The degree of micro-mixing is extracted from the probed development of hydrogen bonds, an interaction

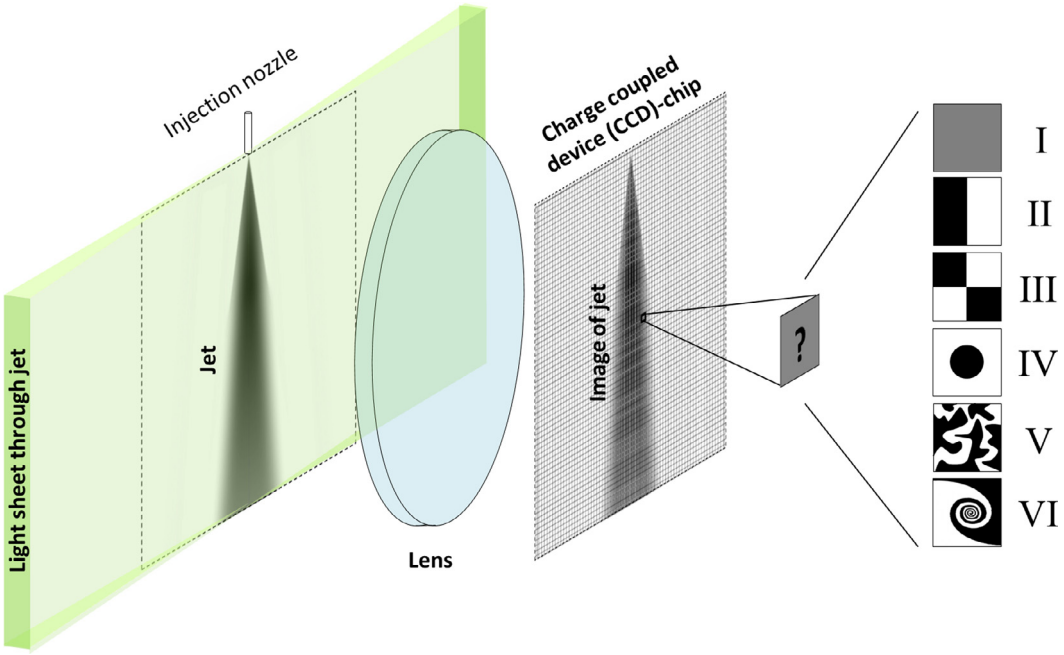

Fig. 1. A real jet is irradiated by a light sheet and the irradiated cross section is imaged via one lens on a charge coupled device (CCD)-detector. Due to the limited spatial resolution, different kinds of micro-mixed structure (I–VI) would all result in the same pixel value, as in all these cases the amount of black and white fluid is identical.

mechanism taking place on the molecular level. Therefore, it has to be underlined that the proposed technique only works for fluids which develop hydrogen bonds, such as typically water, alcohols or amines. The circumstance that water and alcohols are frequently used fluids in chemistry makes this technique applicable to many real and relevant processes. It is also applicable for the investigation into micro- and macro-mixing between liquids, instead of compressed fluids.

The sections that follow will describe the experiment, the evaluation procedure of the acquired Raman spectra and will discuss the results.

2. Materials and procedures

2.1. Materials

Carbon dioxide (CO_2) with a purity of 99.9% and ethanol with a purity of 99.995% were delivered by Linde Company (Germany) and VWR Company (Germany), respectively. Both substances were delivered as a liquid.

2.2. Experimental setup and methods

Fig. 2 shows a sketch of the setup including the Raman experiment and the high pressure mixing chamber.

The mixing chamber is optically accessible via four glass windows. Four heating cartridges inserted into the chamber's main body assure the temperature conditioning. Ethanol (EtOH) and CO_2 enter the chamber preheated to the set operational temperature (usually 313 K) through a coaxial-like capillary type. Here ethanol is injected through the center capillary, while CO_2 flows parallel to the center capillary in seven channels surrounding the center ethanol capillary. Ethanol is fed with a flow rate of 0.021 mol $(min)^{-1}$ using one Teledyne ISCO high-pressure high-precision pump and CO_2 is fed with a flow rate of 2.026 mol $(min)^{-1}$ using two Teledyne ISCO high-pressure high-precision pumps operated in the continuous flow mode. In detail, the CO_2 is dosed as a liquid, as the pump heads are cooled to 274 K. Before the ethanol and the CO_2 enter the high-pressure chamber, both fluids flow each through a 4 m long temperature controlled pipe in order to accommodate them to the set chamber temperature. Thus, the overall molar composition inside the chamber is $x_{CO2} = 0.99$. The CO_2/ethanol mixture exits the chamber at the bottom. A pressure regulator (control valve from Research Control) mounted down-flow the chamber's exit keeps the pressure constant at the set operation pressure. During the calibration experiments the composition of the mixture inside the chamber was varied and the mixture was circulated through the chamber to assure perfect mixing on a macro- and micro-scale. The inner diameter of the ethanol capillary is 500 μm. The chamber is positioned on a motor-driven three-axis high-precision linear stage.

As excitation source we used a long-pulse Nd:YAG laser (Agilite Series Continuum) with a pulse duration (flat top) of 1 μs, a single-shot pulse energy of 1.5 J and a repetition rate of 5 Hz at an emission wavelength of 532 nm. The laser beam was first expanded with a telescope and then focused into the center of the ethanol jet. The focal beam waist is imaged in a right–angle configuration with two achromatic 2″ lenses (f = 200 mm) onto the horizontally orientated entrance slit of an upright standing imaging spectrometer (Andor Shamrock 303i). A long-pass filter positioned in between the two lenses eliminated all signal wavelengths shorter than 550 nm. The imaging spectrometer preserves the spatial information along the horizontal axis and spectrally disperses the signals (> 550 nm) along the vertical axis. Thus, the charge coupled device (CCD)-camera (Andor Newton) mounted at the spectrometers exit detects the Raman scattered photons as a function of their origin (spatial coordinate and horizontal axis of the camera chip) and their energy (spectral coordinate and vertical axis of the camera chip). The CCD-chip of the camera features 400 times 1600 pixels. Each pixel has a size of 16 times 16 μm^2. Therefore theoretically Raman spectra from 400 locations along the laser beam waist (6.4 mm) can be recorded each composed of 1600 pixel data points. In order to improve the signal-to-noise ratio we binned 5 and 2 along the spatial and the spectral axis, respectively. Thus we spatially resolved the 6.4 mm long beam waist in 80 increments of 80 μm length each. The diameter of the beam waist can be

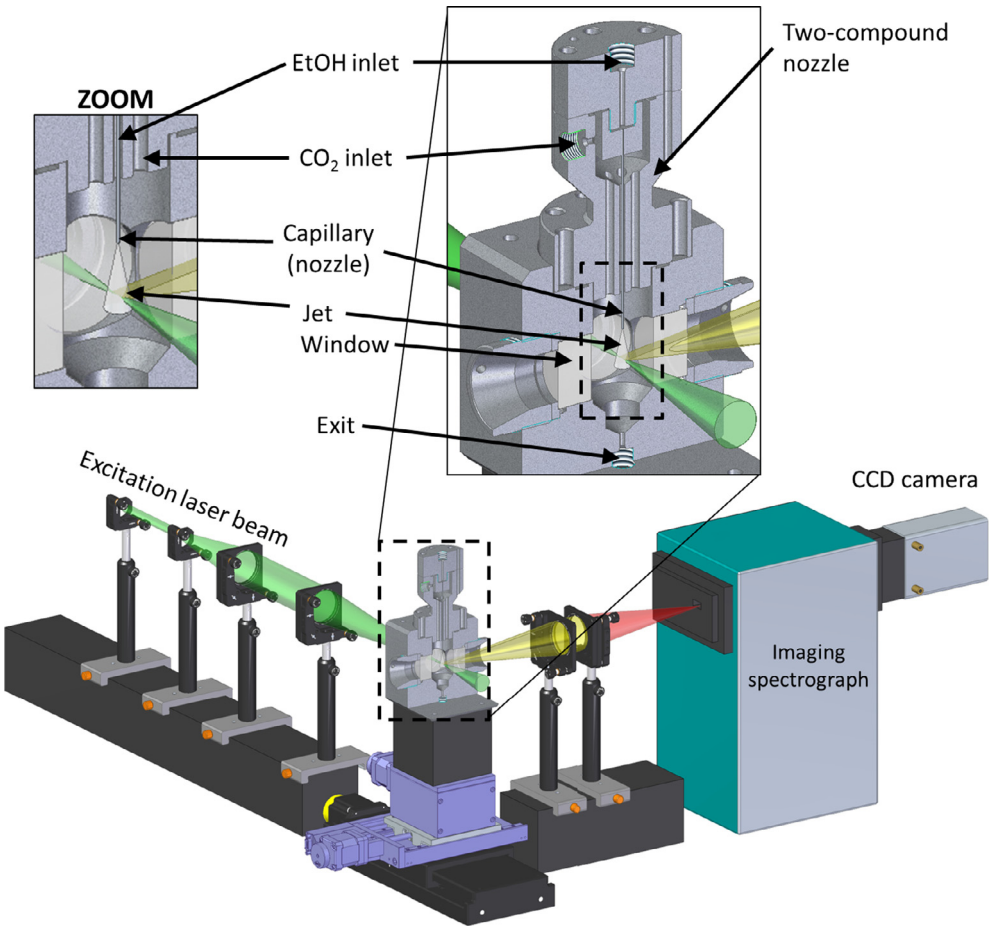

Fig. 2. Sketch of the experimental setup showing the optically accessible high-pressure injection chamber and the excitation as well as the signal paths of the one-dimensional Raman experiment (EtOH: ethanol).

approximated to be 100 µm. One Raman spectrum covers Raman shifts from 800 cm^{-1} to 3700 cm^{-1} and is resolved in 800 data points.

In order to realize Raman measurements at different distances from the capillary exit, the chamber was moved, while the Raman experiment was kept fix.

3. Results and discussion

First, we made calibration measurements in well-mixed CO_2/ethanol mixtures of known composition at 313 K and 10 MPa. In this case the chamber was operated in batch mode. With the exit valve closed, defined amounts of CO_2 and ethanol were fed into the chamber using high-precision high-pressure ISCO pumps. Then also the inlet valves of the chamber were closed and the mixture inside was homogenized by circulating it with a circulation pump through a bypass from the bottom of the vessel to its top. We modified the composition of the mixture by varying the amounts of CO_2 and ethanol we fed into the chamber.

Fig. 3 shows a Raman spectrum of a CO_2/ethanol mixture, homogeneously mixed on the macro- and the micro-scale, with a CO_2 molar fraction of $x_{CO2} = 0.42$ at 313 K and 10 MPa. The Raman spectrum of the mixture contains Raman signals originating from CO_2 and from ethanol (EtOH). The dominant Raman signal feature between 2540 cm^{-1} and 3000 cm^{-1} contains various peaks originating from the C—H vibrations, which has to be assigned to ethanol. We refer to the area under the peak assemble highlighted in orange in Fig. 3 as the ethanol Raman signal intensity I_{EtOH}. All Raman spectra are normalized to I_{EtOH}. The CO_2 Raman signal Fermi dyad is highlighted in red and spectrally overlaps with the other Raman signatures of ethanol. The CO_2 Fermi dyad can be isolated from the mixture spectrum using a spectrum deconstruction method (Schuster et al., 2014; Alsmeyer et al., 2004). We refer to the area under the Fermi dyad as the CO_2 Raman signal intensity I_{CO2}. The spectral region between 3000 cm^{-1} and 3650 cm^{-1} shows the Raman signals coming from the O—H vibration of the hydroxyl group of ethanol. Therefore we refer to the intensity of the O—H vibration as I_{OH}. Unlike the CO_2 or the ethanol Raman signal peaks, the O—H Raman signal is a rather broad band. One single ethanol molecule can develop hydrogen bonds to more or less other ethanol molecules in its vicinity, which influences the vibrational energy of its hydroxyl group. Thus, the broad band accounts for the fact that the hydroxyl groups of different ethanol molecules vibrate with different energies, which is the result of the development of hydrogen bonds between the hydroxyl groups of the ethanol molecules (Kazarian et al., 1993; Knauer et al., 2011). Again, we use a spectrum deconstruction method for the isolation of the O—H Raman signal band I_{OH} from the overlapping ethanol peak assemble I_{EtOH}. On this account the O—H Raman signal band is deconstructed in six Gaussian peaks, which are shown in Fig. 3, and the ethanol peak assemble in four Gaussian peaks, which are not shown in Fig. 3.

The number of peaks used for the deconstruction of the O—H Raman band is not relevant for the further progress of this manuscript, as we do not assign them to specific configurations

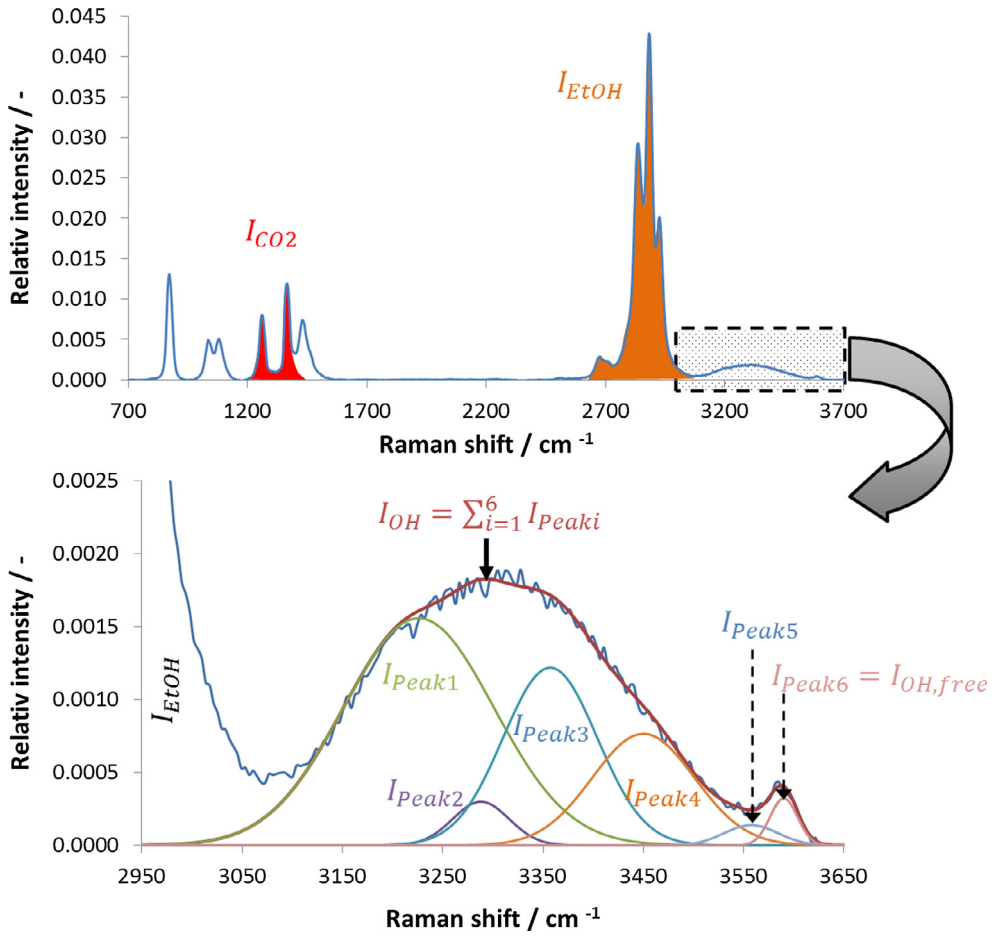

Fig. 3. Raman spectrum of a CO_2/ethanol mixture with a CO_2 molar fraction of $x_{CO2} = 0.42$ at 10 MPa and 313 K. The Raman shift region showing between 3000 and 3650 cm^{-1} the hydroxyl vibration I_{OH} of ethanol is presented in an enlarged insert. The hydroxyl vibration band is deconstructed into six Gaussian peaks.

of hydrogen bonded networks. There is other literature using different and the same number of peaks (Walrafen, 1975, 1962; Castner et al., 1995; Carey and Korenowski, 1998; Sutherland, 1933). Here we use six peaks, as with this number of peaks we obtained the best reproducibility of the entire experimentally measured O—H Raman signal band. Nevertheless, it is of outmost importance that the peak at the right border of the O—H Raman signal band at 3600 cm^{-1} is properly represented by a specific peak, here "Peak 6". "Peak 6" can be assigned to the O—H vibration of the hydroxyl group of an ethanol molecule which does not develop any hydrogen bonds (Barlow et al., 2002; Sokolova et al., 2006; Schuster et al., 2016). Therefore "Peak 6" is also called the Raman signal of "free" hydroxyl groups or that of ethanol monomers $I_{OH,\ free}$. In ethanol vapor at ambient pressure, for example, the distance between ethanol molecules is so large that no hydrogen bonds can develop between them. Therefore the O—H vibration Raman signal of ethanol vapor would only show "Peak 6". The intensities of the "Peak 1" to "Peak 5" would all be zero for ethanol vapor. In the liquid phase the distance between ethanol molecules is short and thus hydrogen bonds can develop and therefore the O—H Raman signal band is broad. In the CO_2/ethanol mixture $x_{CO2} = 0.42$ only a small portion of the hydroxyl groups vibrate freely (not influenced by hydrogen bonds to other molecules), which is represented by the small "Peak 6". Fig. 4 shows how the Raman signatures of CO_2 and ethanol change with the composition of the CO_2/ethanol mixture. Each spectrum is normalized to I_{EtOH}. The higher the CO_2 content is in the mixture, the more pronounced I_{CO2} gets and the more hydroxyl groups vibrate freely, which is shown by the increase of $I_{OH,\ free}$ ("Peak 6").

Having made these calibration measurements in defined mixtures, we can correlate the CO_2 Raman signal intensity fraction R_{CO2} with the mixture's composition x_{CO2},

$$R_{CO2} = \frac{I_{CO2}}{I_{CO2} + I_{EtOH}} = \frac{k_{CO2} n_{CO2}}{k_{CO2} n_{CO2} + k_{EtOH} n_{EtOH}} = \frac{1}{1 + \frac{k_{EtOH} n_{EtOH}}{k_{CO2} n_{CO2}}}$$
$$= \frac{1}{1 + k \cdot \frac{n_{EtOH}}{n_{CO2}}} = \frac{1}{1 + k \cdot \frac{n(1 - x_{CO2})}{n \cdot x_{CO2}}} = \frac{1}{1 + k \cdot \left(\frac{1}{x_{CO2}} - 1\right)} = R_{macro} \quad (2)$$

where k_{CO2}, k_{EtOH} and k are proportionality constants and n_{CO2} and n_{EtOH} are the amounts of substance of CO_2 and ethanol, respectively. As the Raman signal intensities I_{CO2} and I_{EtOH} do not depend on the development of intermolecular interactions, but mainly on the amount of substance of CO_2 and ethanol in the mixture, we refer in the further progress to it as the quantity R_{macro} and use this quantity for measuring the composition of a mixture on the macro-scale.

On the contrary, $I_{OH,\ free}$ depends on the development of hydrogen bonds and thus contains information about the degree of mixing on the micro-scale. We therefore correlate empirically the "free" hydroxyl group Raman signal intensity ratio $R_{OH,\ free}$ with the mixture composition x_{CO2}

$$R_{OH,free} = \frac{I_{OH,free}}{I_{EtOH}} = R_{micro} \propto \frac{n_{OH,free}}{n_{EtOH}} = f(x_{CO2}) \quad (3)$$

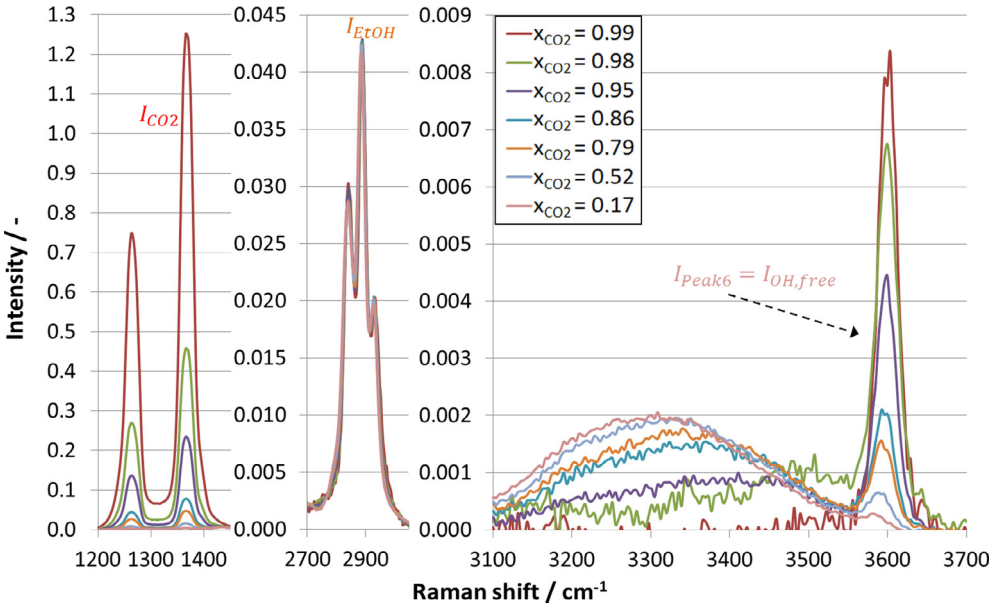

Fig. 4. Raman spectra of CO_2/ethanol mixtures of different composition at 313 K and 10 MPa.

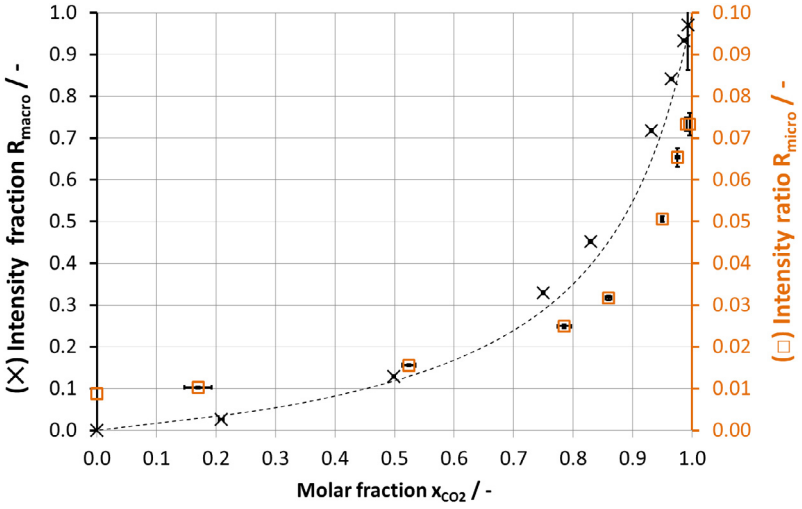

Fig. 5. Calibration curves of R_{macro} (X) and R_{micro} (□) as a function of the CO_2/ethanol mixture composition x_{CO2} at 10 MPa and 308 K in mixtures mixed homogeneously on the macro- and the micro-scale.

and in the further progress refer to it as R_{micro}, as it contains information about the degree of mixing on the micro-scale. Fig. 5 shows the experimentally measured R_{macro} (X) and R_{micro} (□) as a function of the set mixture composition x_{CO2}. It must be underlined again that the curves provided in Fig. 5 result from calibration measurements carried out in mixtures homogenous on the macro- and the micro-scale. The dotted line represents Eq. (2) as best fit to R_{macro} with $k = 7.41$. Each data point is the mean of 150 single measurements. The error bars represent the standard deviation of the 150 measurements and for some data points smaller than the symbol representing the data point.

Both curves rise with increasing molar fractions. During the calibration measurements the mixtures were mixed perfectly on the macro- as well as on the micro-scale, such as in case I in Fig. 1. Therefore, vice versa, one can read the composition of an unknown CO_2/ethanol mixture in Fig. 5 from either R_{macro} or R_{micro} as long as these mixtures are also perfectly mixed on the macro- and on the micro-scale. Then, both approaches will result in the same mixture composition $x_{CO2,macro} = x_{CO2,micro}$. But, assuming a mixture such as cases II-VI in Fig. 1, R_{macro} and R_{micro} would reveal different mixture compositions $x_{CO2,macro} \neq x_{CO2,micro}$. The black fluid ethanol (eddy) is not yet mixed with the white fluid CO_2. Thus, the hydrogen bonds between the ethanol molecules in the black micro-structures are developed as they are developed in pure ethanol. Therefore, if the mixture contains equal portions of ethanol and CO_2, the R_{macro} calibration curve would provide $x_{CO2,macro} = 0.5$. But the R_{micro} calibration curve would provide $x_{CO2,micro} = 0$, as the hydrogen bonds are developed as they are developed in pure ethanol. Summarizing, the comparison of $x_{CO2,macro}$ and $x_{CO2,micro}$ quantifies the lag between the mixing progresses on a micro- and on a macro-scale. We therefore can now use the calibration curves shown in Fig. 5 for the analysis of macro- and micro-mixing in the high-pressure injection experiment. In detail we use as empirical best fits to the experimental calibration results

$$R_{macro} = 3.77x_{CO_2}^6 - 6.31x_{CO_2}^5 + 3.87x_{CO_2}^4 - 0.75x_{CO_2}^3 + 0.35x_{CO_2}^2 + 0.06x_{CO_2} \quad (4)$$

$$R_{micro} = 2.65x_{CO_2}^6 - 6.59x_{CO_2}^5 + 6.11x_{CO_2}^4 - 2.56x_{CO_2}^3 + 0.48x_{CO_2}^2 - 0.02x_{CO_2} + 0.01 \quad (5)$$

and also use these fit equations for the computation of $x_{CO2,macro}$ and $x_{CO2,micro}$ from R_{macro} and R_{micro}.

From now on the high-pressure injection chamber is operated in continuous mode. The ethanol is injected continuously through the capillary into the chamber, while also the CO_2 is fed continuously and coaxially to the injection chamber from the top into the chamber. The CO_2/ethanol mixture exits continuously through the chamber's bottom outlet, while the temperature and the flow rates are kept constant at 313 K, 2.026 mol $(min)^{-1}$ for CO_2 and 0.0205 mol $(min)^{-1}$ for ethanol. Fig. 6 shows the center cross sections of ethanol sprays/jets injected into the high-pressure chamber at various chamber pressures. The photographs were made with a Raman imaging experimental setup, which is described in the "supporting information". The photographs were made with an exposure time of 1 µs which is short enough to make snapshots of the sprays/jets. The photographs are supposed to give a general impression about the sprays/jets and the flow structures, rather than quantitative information, and have therefore not been corrected for the laser beam profile, laser beam attenuation or multiple scattering.

For pressures below 9 MPa the occurrence of distinct drops/ligaments documents a two-phase spray mixing process governed by the evaporation of the dispersed liquid phase into the compressed bulk-phase and by the dissolution of the compressed bulk-phase into the dispersed liquid phase. At pressures above 8.5 MPa the absence of drops but the presence of turbulent structures and gradients documents a single-phase jet mixing process governed by macro- and micro-scale mixing. This is due to the circumstance that 9 MPa are above the mixture critical pressure of the binary system CO_2/ethanol at 313 K (De Marco et al., 2015). Therefore we focused our investigations on the pressure of 10 MPa where the mass transport is dominated by mixing and not by evaporation and dissolution (Lengsfeld et al., 2000).

Fig. 7 shows on the left side a mean image of the ethanol jet's cross section averaged from 75 snapshots (Raman images), as one of them is shown in Fig. 6. This mean image again is only provided in order to give to the reader a general impression about the appearance of the continuous jet. Again it is not corrected for the laser beam profile, laser attenuation or multiple scattering. On the right side the mixture compositions $x_{CO2,macro}$ and $x_{CO2,micro}$ are given as a function of the distance from the injection nozzle. They were computed from the Raman spectra acquired with the Raman line imaging setup shown in Fig. 2 and evaluated based on the two calibration curves shown in Fig. 5 and specified in Eqs. (4) and (5). Each data point is the mean of 75 measurements with the error bars (shaded regions) showing their standard deviation. Directly at the capillary exit we find pure ethanol $x_{CO2,macro} = x_{CO2,micro} = 0$. Further downstream the composition of the mixture gets richer in CO_2, which is reflected first ($z = 2$ mm) by the increase of $x_{CO2,macro}$ and later ($z = 4$ mm) by the increase of $x_{CO2,micro}$.

Three millimeters downstream the capillary exit $x_{CO2,macro} = 0.15$ quantifies that already 15% of the amount of substance of the mixture is CO_2, while $x_{CO2,micro} \approx 0$ does not yet detect the presence of considerable amounts of CO_2. Therefore we assume that the first CO_2 detected on the jet center line must have been entrained (macro-mixed), but not diffused (micro-mixed)! If it diffused there, the degree of mixing on both scales would have been the same. Thus, the entrainment of CO_2 is responsible for the initial lag of micro-mixing behind macro-mixing. This lag,

$$lag = x_{CO_2,macro} - x_{CO_2,micro} \quad (6)$$

represented by the triangle data points, reaches its maximum between $z = 4$ mm and $z = 5$ mm. Further downstream the lag between macro- and micro-mixing further decreases until the macro- and the micro-scale mixing degrees become identical at approximately $z = 11$ mm. We can conclude that as long as the lag between micro- and macro-mixing increases $z < 4$ mm, more CO_2 is entrained into the jet than at the same time can be mixed on the micro-scale with ethanol due to diffusion. And, once the lag between micro- and macro-mixing decreases $z > 5$ mm, more CO_2 is mixed with ethanol on the micro-scale due to diffusion than at the same time is entrained into the jet's center. The entrainment weakens with increasing axial distance from the nozzle exit.

Fig. 8 shows radial macro- $x_{CO2,macro}$ and micro-scale composition profiles $x_{CO2,micro}$ for axial distances from the capillary exit of $z = 0$ mm, $z = 5$ mm and $z = 10$ mm of the same jet which was shown as a mean photograph on the left side in Fig. 7. Directly

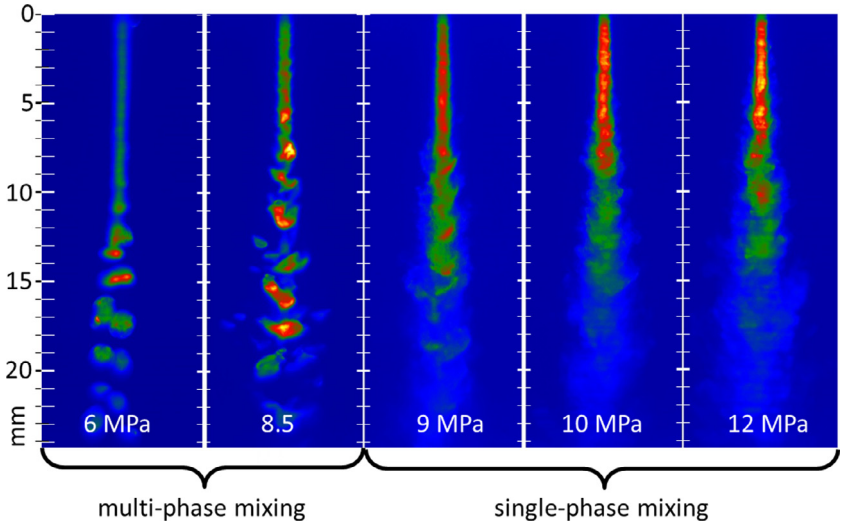

Fig. 6. Photographs of the center cross sections of the ethanol spray/jet in compressed CO_2 at 313 K but different pressures. The cross sections were visualized exciting the spray cross section with a laser light sheet and by detecting the Raman signals of ethanol with a camera.

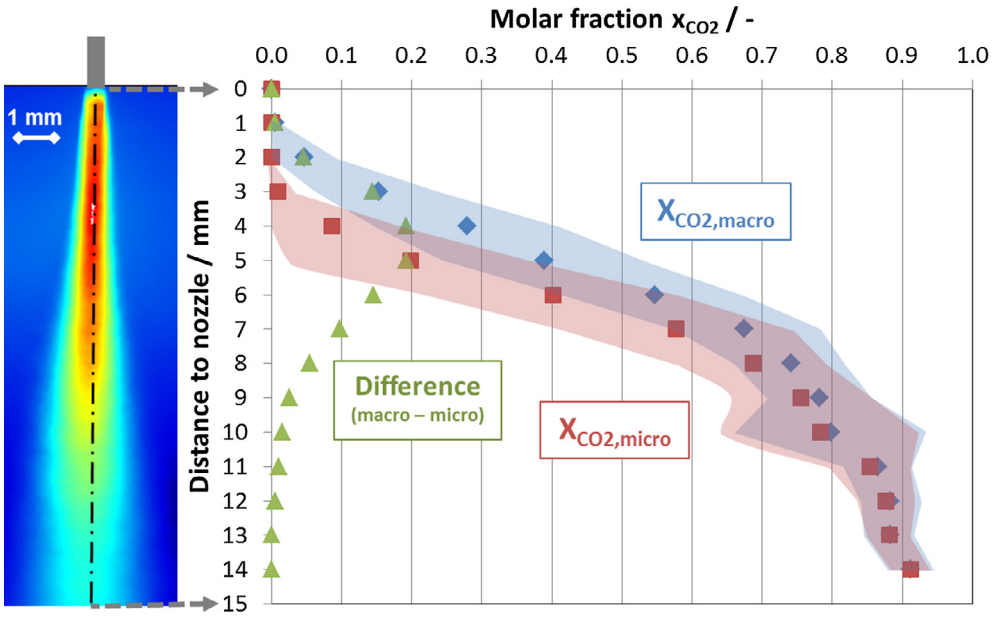

Fig. 7. (left) Mean of 75 snapshot photographs (Raman imaging) and (right) macro- $x_{CO2,macro}$ and micro- $x_{CO2,micro}$ scale mixture composition as a function of the distance from the capillary exit along the axial jet center line (10 MPa, 313 K).

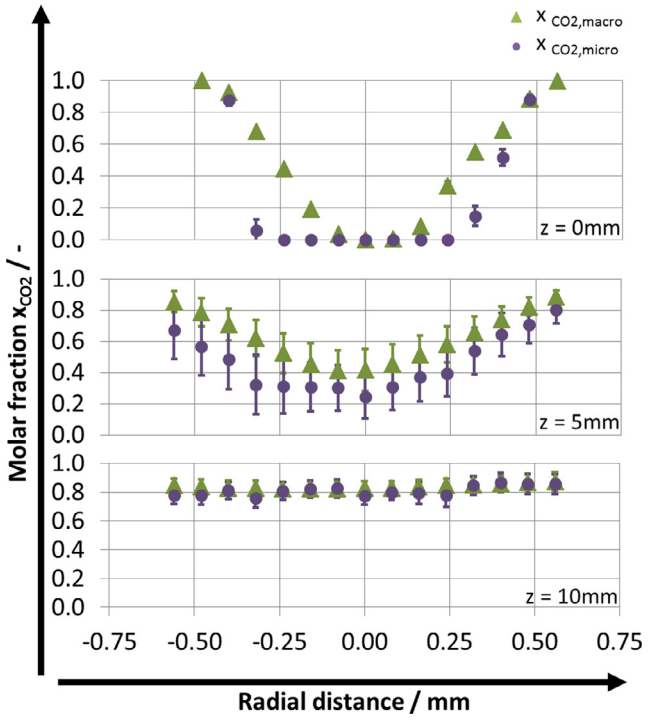

Fig. 8. Radial macro- $x_{CO2,macro}$ and micro-scale mixture composition $x_{CO2,micro}$ profiles at axial distances from the capillary exit of $z = 0$ mm, $z = 5$ mm and $z = 10$ mm.

underneath the capillary exit $z = 0$ mm the micro-scale composition profile $x_{CO2,micro}$ shows a broader jet core than the macro-scale composition profile $x_{CO2,macro}$. Remember that the inner diameter of the capillary is 500 µm, which is pretty close to the jet core diameter extractable from the micro-scale composition profile $x_{CO2,micro}$, but not from the macro-scale composition profile $x_{CO2,macro}$. Therefore we conclude that already directly underneath the capillary exit some CO_2 is entrained into the boundary areas of the jet. The respective boundary areas are then mixed on a macro-scale (entrainment), but not yet on a micro-scale (diffusion). Further downstream the capillary exit ($z = 5$ mm) both composition profiles show a certain progress of mixing and a similar profile shape. Again micro-mixing is behind macro-mixing $x_{CO2,micro} < x_{CO2,macro}$. Again the lag between the mixing progress on the macro- and on the micro-scale has to be explained by the entrainment of CO_2 into the jet. At the outer regions of the jet the composition lag on the micro- and on the macro-scale is smaller than in the jet core regions.

Due to the high density of the bulk CO_2-rich phase the outer regions of the jet are decelerated rapidly and a velocity profile develops which is slow at the jet boundary and fast in the jet center. Consequently, at a constant distance downstream the capillary exit (here $z = 5$ mm) the mixture elements in the jet core feature a shorter residence time than those at the boundary of the jet. Thus, at the outer jet boundary diffusion had more time to mix the mixture on the micro-scale.

In a distance of $z = 10$ mm downstream the capillary exit the composition profiles on the macro- and on the micro-scale are very similar, with respect to the values of $x_{CO2,macro}$ and $x_{CO2,micro}$, and are rather flat. Here diffusion largely degraded the lag between macro- and micro-mixing over the entire radial jet profile. Mixing is not yet completed, as – with respect to the amounts of ethanol and CO_2 fed to the chamber – we adjusted a composition of $x_{CO2} = 0.99$, which we did not measure at $z = 10$ mm. Fig. 7 shows that also in a distance of $z = 15$ mm the mixing progress is still ongoing.

4. Conclusions and perspectives

We here introduced a one-dimensional measurement technique, which can probe simultaneously the degree of mixing progress on the macro- (flow mixing) and the micro-scale (diffusion), spatially and temporally resolved along a line. One can use the introduced technique for analyzing the influence of micro-scale mixing onto the processes that follow mixing and likewise take place on the micro-scale, such as reaction or precipitation. We demonstrated that the measurement technique can reveal the lag between the progress of micro- and macro-mixing

in a jet-mixing experiment, where liquid ethanol is injected in a compressed CO_2-rich bulk-phase. As the analysis of the mixing progress on the micro-scale relies on measuring the development of hydrogen bonds – here between the ethanol molecules –, we are confident that it also can be applied to measure the degree of micro-mixing in other single-phase mixing experiments where at least one compound can develop hydrogen bonds, such as water, alcohols or amines. Therefore we see a wide range of application areas from processes using water as solvent or reacting medium to processes where alcohols are combusted directly or upgraded to biodiesel, the measurement strategy can also be realized in a zero-dimensional back scattering configuration. Then it would be suitable for measurements on objects featuring only one optical access or where it is simply more practical to measure in a back scattering configuration such as in microfluidic devices. But, if cameras equipped with suitable bandpass filters are used instead of the spectrometer, one would also be able to detect two-dimensional (spatially resolved) snapshots of the mixing progress on the micro- and the macro-scale. Of course in this case the excitation laser beam then would have to be formed to a light sheet instead of a thin beam waist along the laser beam focus.

Acknowledgments

The project leading to these results/applications has received funding from the European Union's Horizon 2020 research and innovation program under grant agreement No. 637654 (Inhomogeneities). Furthermore the authors gratefully acknowledge the funding of the Erlangen Graduate School in Advanced Optical Technologies (SAOT) by the German Research Foundation (DFG) in the framework of the German excellence initiative.

Appendix A. Supplementary material

Supplementary data associated with this article can be found, in the online version, at http://dx.doi.org/10.1016/j.ces.2017.01.034.

References

Alsmeyer, F., Koß, H.-J., Marquardt, W., 2004. Indirect spectral hard modeling for the analysis of reactive and interacting mixtures. Appl. Spectrosc. 58, 975–985.
Baldyga, J., Bourne, J.R., 1989. Simplification of micromixing calculations. II. New applications. Chem. Eng. J. 42, 93–101.
Bałdyga, J., Bourne, J.R., 1999. Turbulent Mixing and Chemical Reactions. Wiley.
Barlow, S.J., Bondarenko, G.V., Gorbaty, Y.E., Yamaguchi, T., Poliakoff, M., 2002. An IR study of hydrogen bonding in liquid and supercritical alcohols. J. Phys. Chem. A 106, 10452–10460.
Braeuer, A., Dowy, S., Torino, E., Rossmann, M., Luther, S.K., Schluecker, E., Leipertz, A., Reverchon, E., 2011. Analysis of the supercritical antisolvent mechanisms governing particles precipitation and morphology by in situ laser scattering techniques. Chem. Eng. J. 173, 258–266.
Braeuer, A., Adami, R., Dowy, S., Rossmann, M., Leipertz, A., 2011. Observation of liquid solution volume expansion during particle precipitation in the supercritical CO_2 antisolvent process. J. Supercrit. Fluids 56, 121–124.
Carey, D.M., Korenowski, G.M., 1998. Measurement of the Raman spectrum of liquid water. J. Chem. Phys. 108, 2669–2675.
Castner, E.W., Chang, Y.J., Chu, Y.C., Walrafen, G.E., 1995. The intermolecular dynamics of liquid water. J. Chem. Phys. 102, 653–659.
Davidson, P.A., 2004. Turbulence. Oxford University Press, Oxford.
De Marco, I., Rossmann, M., Prosapio, V., Reverchon, E., Braeuer, A., 2015. Control of particle size, at micrometric and nanometric range, using supercritical antisolvent precipitation from solvent mixtures: application to PVP. Chem. Eng. J. 273, 344–352.
Falgout, Z., Rahm, M., Sedarsky, D., Linne, M., 2016. Gas/fuel jet interfaces under high pressures and temperatures. Fuel 168, 14–21.
Kazarian, S.G., Gupta, R.B., Clarke, M.J., Johnston, K.P., Poliakoff, M., 1993. How is hydrogen-bonding influenced by solvent density? The spectroscopic study and modeling of the interaction between a proton donor and acceptor from the gas phase to supercritical fluid states. J. Am. Chem. Soc. 115, 11099–11109.
Kling, K., Mewes, D., 2004. Two-colour laser induced fluorescence for the quantification of micro- and macromixing in stirred vessels. Chem. Eng. Sci. 59, 1523–1528.
Kluge, J., Fusaro, F., Casas, N., Mazzotti, M., Muhrer, G., 2009. Production of PLGA micro- and nanocomposites by supercritical fluid extraction of emulsions: I: Encapsulation of lysozyme. J. Supercrit. Fluids 50, 327–335.
Knauer, O.S., Lang, M.C., Braeuer, A., Leipertz, A., 2011. Simultaneous determination of the composition and temperature gradients in the vicinity of boiling bubbles in liquid binary mixtures using one-dimensional Raman measurements. J. Raman Spectrosc. 42, 195–200.
Kolmogorov, A.N. The Local Structure of Turbulence in Incompressible Viscous Fluid for Very Large Reynolds Numbers. In: Dokl. Akad. Nauk SSSR, JSTOR; 1941. pp. 301–305.
Koochesfahani, M.M., Dimotakis, P.E., 1986. Mixing and chemical reactions in a turbulent liquid mixing layer. J. Fluid Mech. 170, 83–112.
Lehwald, A., Thévenin, D., Zähringer, K., 2010. Quantifying macro-mixing and micro-mixing in a static mixer using two-tracer laser-induced fluorescence. Exp. Fluids 48, 823–836.
Lengsfeld, C.S., Delplanque, J.P., Barocas, V.H., Randolph, T.W., 2000. Mechanism governing microparticle morphology during precipitation by a compressed antisolvent: atomization vs. nucleation and growth. J. Phys. Chem. B 104, 2725–2735.
Liparoti, S., Adami, R., Reverchon, E., 2015. Supercritical assisted atomization: effect of operative conditions on PVP microparticle size and morphology. J. Supercrit. Fluids 97, 31–35.
Mayer, W., Schik, A., Schäffler, M., Tamura, H., 2000. Injection and mixing processes in high-pressure liquid oxygen/gaseous hydrogen rocket combustors. J. Propul. Power 16, 823–828.
Meier, T., Stathopoulos, P., Rudolf von Rohr, P., 2016. Hot surface ignition of oxygen–ethanol hydrothermal flames. J. Supercrit. Fluids 107, 462–468.
Michaeli, W., Heinz, R., 2000. Foam extrusion of thermoplastic polyurethanes (TPU) using CO_2 as a blowing agent. Macromol. Mater. Eng. 284–285, 35–39.
Queiroz, J.P.S., Bermejo, M.D., Mato, F., Cocero, M.J., 2015. Supercritical water oxidation with hydrothermal flame as internal heat source: efficient and clean energy production from waste. J. Supercrit. Fluids 96, 103–113.
Richardson, L., 1922. Weather Prediction by Numericrll Process. Cambridge University Press.
Rothenfluh, T., Schuler, M.J., von Rohr, P.R., 2011. Penetration length studies of supercritical water jets submerged in a subcritical water environment using a novel optical Schlieren method. J. Supercrit. Fluids 57, 175–182.
Roy, A., Joly, C., Segal, C., 2013. Disintegrating supercritical jets in a subcritical environment. J. Fluid Mech. 717, 193–202.
Schuster, J.J., Will, S., Leipertz, A., Braeuer, A., 2014. Deconvolution of Raman spectra for the quantification of ternary high pressure phase equilibria composed of carbon dioxide, water and organic solvent. J. Raman Spectrosc. 45, 246–252.
Schuster, J.J., Siegler, P., Guenther, A., Wirth, K.-E., Braeuer, A., 2016. Simultaneous analysis of the dispersed liquid and the bulk gas phase of water sprays using Raman spectroscopy. Appl. Spectrosc. 70, 1055–1062.
Sokolova, M., Barlow, S.J., Bondarenko, G.V., Gorbaty, Y.E., Poliakoff, M., 2006. Comparison between IR absorption and Raman scattering spectra of liquid and supercritical 1-butanol. J. Phys. Chem. A 110, 3882–3885.
Sutherland, G.B.B.M., 1933. Experiments on the Raman effect at very low temperatures. Proceed. Roy. Soc. Lond. Ser. A, Contain. Papers Math. Phys. Character 141, 535–549.
Walrafen, G.E., 1962. Raman spectral studies of the effects of electrolytes on water. J. Chem. Phys. 36, 1035–1042.
Walrafen, G.E., 1975. Raman spectra from Si–OH groups in solid optical fibers. J. Chem. Phys. 62, 297–298.
Wellig, B., Weber, M., Lieball, K., Prikopsky, K., von Rohr, P.R., 2009. Hydrothermal methanol diffusion flame as internal heat source in a SCWO reactor. J. Supercrit. Fluids 49, 59–70.
Wensing, M., Vogel, T., Götz, G., 2015. Transition of diesel spray to a supercritical state under engine conditions. Int. J. Engine Res. http://dx.doi.org/10.1177/1468087415604281.
Yip, B., Lozano, A., Hanson, R.K., 1994. Sensitized phosphorescence: a gas phase molecular mixing diagnostic. Exp. Fluids 17, 16–23.